JOURNAL OF THE AMERICAN CHEMICAL SOCIETY
Article
Cite This: J. Am. Chem. Soc. 2019, 141, 2111−2121
pubs.acs.org/JACS

Acid Responsive Hydrogen-Bonded Organic Frameworks

Ichiro Hisaki,*,† Yuto Suzuki,‖,‡ Eduardo Gomez,‖,§ Qin Ji,† Norimitsu Tohnai,‡ Takayoshi Nakamura,† and Abderrazzak Douhal*,§

†Research Institute for Electronic Science, Hokkaido University, Kitaku, Sapporo, Hokkaido 001-0020, Japan

‡Department of Material and Life Science, Graduate School of Engineering, Osaka University, 2-1 Yamadaoka, Suita, Osaka 565-0871, Japan

§Departamento de Química Física, Facultad de Ciencias Ambientales y Bioquímica, and INAMOL, Universidad de Castilla-La Mancha, Avenida Carlos III, S/N, 45071 Toledo, Spain

Supporting Information

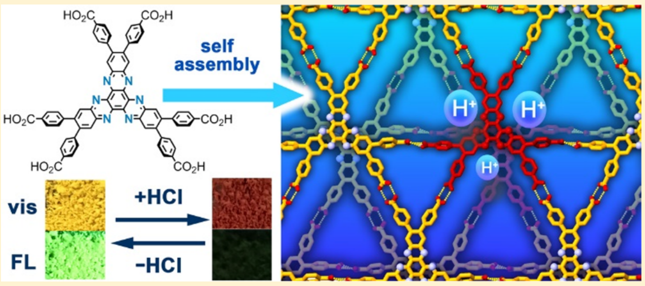

ABSTRACT: A porous hydrogen-bonded organic framework (HOF) responsive to acid was constructed from a hexaazatrinaphthylene derivative with carboxyphenyl groups (**CPHATN**). Precise structures of both 1,2,4-trichlorobenzene solvate [**CPHATN-1(TCB)**] and activated HOF with permanent porosity (**CPHATN-1a**) were successfully determined by single-crystalline X-ray diffraction analysis. Permanent porosity of **CPHATN-1a** was evaluated by gas sorption experiments at low temperature. **CPHATN-1a** also shows significant thermal stability up to 633 K. Its crystals exhibit a rich photochemistry thanks to intramolecular charge-transfer and interunit proton-transfer reactions. Femtosecond (fs) experiments on crystals demonstrate that these events occur in ≤200 fs and 1.2 ps, respectively. Moreover, single-crystal fluorescence microscopy reveals a shift of the emission spectra most probably as a result of defects and a high anisotropic behavior, reflecting an ordered crystalline structure with a preferential orientation of the molecular dipole moments. Remarkably, **CPHATN-1a**, as a result of the protonation of pyradyl nitrogen atoms embedded in its π-conjugated core, shows reversible vapor acid-induced color changes from yellow to reddish-brown, which can be also followed by an ON/OFF of its emission. To the best of our knowledge, this is the first HOF that exhibits acid-responsive color changes. The present work provides new findings for developing stimuli responsive HOFs.

INTRODUCTION

A porous organic framework with well-defined organic components and pores is one of the most attractive functional materials applicable not only for storage and separation of gases and organic molecules but also for organic electronic devices and sensors.[1] Since Yaghi and co-workers reported pioneering works on covalent organic frameworks (COFs),[2] the field of porous organic materials has come to the forefront of science and technologies.[3] The materials built from molecules through hydrogen bonding, known as hydrogen-bonded organic frameworks (HOFs)[4] or supramolecular organic frameworks (SOFs),[5] have also attracted much attention recently because, in contrast to COFs, HOFs are able to be isolated as high-crystalline materials, such as single crystals, in many cases due to their reversible hydrogen-bond formation and dissociation. This allows us to reveal their structures precisely based on single-crystal X-ray diffraction (SXRD) analysis and, therefore, to investigate their structure—property relationship. HOFs can be also regenerable[6] and flexible[7] due to the above-mentioned bond feature. Fragility, on the other hand, has prevented HOFs from being applied as functional porous materials. The structures often collapse during removal of solvent molecules from pores of the solvated frameworks. Furthermore, even when molecular structures and hydrogen-bonding manners are predesigned well, the molecules do not always yield the desired porous HOFs, but result in unexpected nonporous materials. Establishment of a universal design strategy and creation of new functionality, such as external-stimuli responsiveness, are still developing, although a number of HOFs have been reported.[8]

In connection with this, we previously proposed that C_3 symmetric π-conjugated molecules with three *o*-bis(carboxyphenyl)aryl groups in periphery were able to be applied for constructing HOFs[9] and achieved significantly stable HOFs with permanent porosity.[10] To develop external stimuli-responsive fluorescent HOFs with permanent porosity, we next designed a carboxyphenyl-substituted hexaazatrinaphthylene[11] derivative (**CPHATN**) as a building block.

Introducing nitrogen atoms into polycyclic aromatic hydrocarbons allows (1) fine-tuning of frontier orbital levels, lowering LUMO levels in many cases, (2) coordinating with metal cations, and (3) interacting with cationic species such as metal ions, proton, and other organic cations. After establish-

Received: November 11, 2018
Published: January 7, 2019

ment of a facile synthetic route,[12] HATN and its analogues have been widely applied for electron-transporting materials,[13] ligands of novel metal complexes,[14] receptor for cations,[15] catalysts,[16] single-molecular magnets,[17] cathode of lithium batteries,[18] and metal−organic frameworks,[19] in addition for a mesogen of liquid crystals.[20] More recently, HATN segments are used for constructing COFs applicable hydrogen storage,[21] lithium battery,[22] Pb(II) cation scavenger,[23] and catalyst.[24] However, no examples of HOFs based on HATN have been reported so far.

In this work, we report an acid-responsive, extremely thermostable HOF with permanent porosity by using **CPHATN**. We reveal that the **CPHATN** forms a hydrogen-bonded hexagonal network (H-HexNet),[8] which is stacked without interpenetration to give a layered HOF (Figure 1). The HOF can be prepared by facile recrystallization. The activated HOF (**CPHATN-1a**) retains its porous structure up to at least 633 K and is basically stable against common organic solvents. Femtosecond emission spectroscopy indicates that the photobehavior of the excited crystals is shaped by ultrafast intramolecular charge-transfer and proton-transfer events happening in ≤200 fs and 1.2 ps, respectively. Space- and time-resolved fluorescence microscopy shows that cracks and expected defects in the crystals affect the emission spectra and lifetime. We also observed that single crystals exhibit a high anisotropic behavior, reflecting a strongly ordered system. Very interestingly, **CPHATN-1a** changes color reversibly from yellow to reddish-brown when exposed to acids, and its fluorescence can be switched OFF or ON in the presence or removal of acid vapors. This is, to the best of our knowledge, the first example of HOFs with external-stimuli responsiveness in color and emission. The present results would open a door to develop new porous materials with stimuli responsiveness.

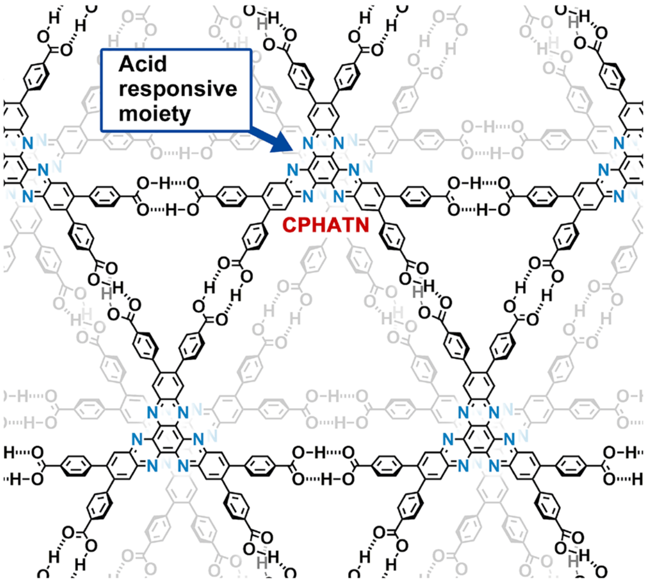

Figure 1. Porous layered assembly of H-HexNets based on HATN derivative (**CPHATN**), which has acid-responsive moieties.

■ RESULTS AND DISCUSSION

Synthesis and Crystallization of CPHATN. 4,5-Bis-(methoxycarboxyphenyl)-1,2-diaminobenzene (**2**) was synthesized by Suzuki−Miyaura cross-coupling reaction of 4,5-dibromo-1,2-diaminobenzene and 4-methoxycarbonylphenylboronic acid (**1**). Diaminobenzene derivative **2** was treated with cyclohexanehexone (**3**) in acetic acid to give ester derivative **4**, which was subsequently hydrolyzed to give **CPHATN** (Scheme 1). Crystallization was preliminarily attempted by using a mixed solution of polar solvent [*N*,*N*-dimethylacetamide (DMAc) or *N*-methylpyrrolidone (NMP)] and aromatic solvent [methyl benzoate (MeBz) or 1,2,4-trichlorobenzene (TCB)] at 333 K, resulting nonporous crystals **CPHATN-NP(DMAc)** and **CPHATN-NP(NMP)** (Figure S1) in which carboxy groups of **CPHATN** are trapped by solvent molecules via hydrogen bonds, preventing formation of a H-HexNet. Finally, slow evaporation of a mixed solution of NMP and TCB at 373 K for 12 h allowed formation of a block-shaped *P*-1 crystal [**CPHATN-1(TCB)**], which has a layered structure of H-HexNet frameworks.

Scheme 1. Synthesis Procedure of Hexaazatrinaphthylene Derivative CPHATN

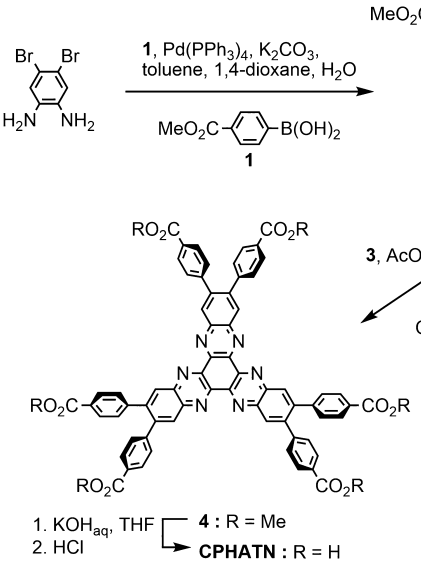

Thermal Behaviors of CPHATN-1(TCB). Thermogravimetric (TG) analysis of **CPHATN-1(TCB)** shows that solvent molecules accommodated in the channel are completely removed at 527 K and the resultant desolvated state is kept up to ca. 673 K (Figure 2a). The weight loss of 22% indicates that **CPHATN-1(TCB)** contains TCB with a host−guest ratio of 1:2 (calcd 24.7%). Next, to reveal structural changes of **CPHATN-1(TCB)** during desolvation by heating, we recorded variable-temperature powder X-ray diffraction (VT-PXRD) patterns of as-formed crystalline bulks of **CPHATN-1(TCB)** from room temperature to 633 K, which is the upper limit temperature of the apparatus we used (Figure 2b). Although the initial patterns are not clear due to bulk solvent attached on the crystalline surface and severe disorder of solvent molecules accommodated in voids, peaks gradually appear with heating. Weak but unambiguous peaks at 4.30, 5.18, 8.62, and 10.48° start to appear at 356 K, and these peaks are slightly shifted into wider angle up to 387 K, indicating subtle shrinkage of the crystallographic cell. The peak intensity increased as heating reaches a plateau at ca. 523 K and remains up to 633 K (Figure 1b,c). These results indicate that the desolvated framework is stable and rigid sufficiently to retain the structure under high temperature.

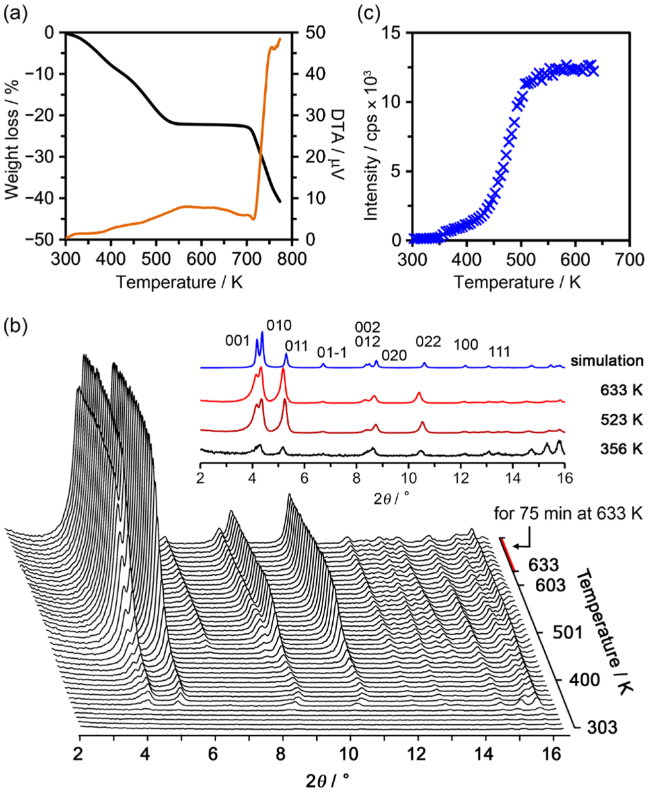

Figure 2. Thermal behavior of crystalline bulk of as-formed **CPHATN-1(TCB)**. (a) TG-DTA profile of **CPHATN-1(TCB)**. (b) VT-PXRD measurements of **CPHATN-1(TCB)** heated from room temperature to 633 K. Insets: typical PXRD patterns during heating. (c) Changes of the 010 peak intensity with temperature. For VT-PXRD measurements, the temperature was raised at a rate of 1 K/min. PXRD patterns were recorded from 2° to 17° of 2*θ* with the scan rate of 3°/min. Therefore, each scan has a temperature gradient of 5 K. *λ* = 1.54187 Å.

Judging from the thermal behavior of the framework mentioned above, activation of **CPHATN-1(TCB)** was accomplished by heating at 463 K for 72 h under vacuum conditions, giving the corresponding desolvated material **CPHATN-1a** possessing permanent porosity. Complete desolvation and crystallinity of the activated material were confirmed by ^{1}H NMR spectra of solutions dissolved in deuterated DMSO (Figure S2) and PXRD patterns (Figure S3), respectively. Desolvation of **CPHATN-NP(NMP)** under the same conditions also gives the similar desolvated framework judging from the PXRD pattern, although its crystallinity is lower (Figure S4).

Crystal Structures of CPHATN-1(TCB) and CPHATN-1a. In *P*-1 crystal **CPHATN-1(TCB)**, *o*-bis(carboxyphenyl)-benzene moieties form a triangular hydrogen-bonded motif so-called phenylene triangle (PhT) motif[8] to give a hydrogen-bonded hexagonal network (H-HexNet) sheet, which then stacks without interpenetration to give a layered assembly of H-HexNet (Figure 3a). The **CPHATN** core is slightly deformed due to packing force: root-mean-square deviation (RMSD) of the **CPHATN** core is 0.142 Å. An H-HexNet layer tightly stacks with the adjacent layers in two ways (Figure 3b). A **CPHATN** core in the first layer (yellow) stacks tightly with a core in the second layer (cyan) with a N···N distance of 3.08 Å. Interplanar distances between mean planes of the stacked **CPHATN** cores is 2.90 Å. The other stacking pattern is that the cores in the second (cyan) and third (dark blue) layers are overlapped between edges of the cores: the interplanar distances is 3.13 Å. The framework has a one-dimensional channel along the crystallographic *a* axis, and TCB molecules used for crystallization are accommodated in the channel, although they are severely disordered and, therefore, are not able to be solved crystallographically. A ratio of total potential solvent area volume calculated by PLATON software was 26% (cell volume: 3190.3 Å^3, void volume per cell: 843.0 Å^3).

It is noteworthy that the material after activation partly retain single crystallinity, allowing us to accomplish SXRD analysis of **CPHATN-1a**. As shown in Table 1, mainly the length of the *b* axis is shortened by 1.4 Å, and the *γ* becomes smaller by 4.3°. The refined structure is shown in Figure 3d−g. These changes in the cell parameters are brought particularly from deformation in the carboxy dimers having conformational frustration[9a,b] (for more details, see Figure S5), while relative positions of the stacked **CPHATN** cores remains (Figure 3c,f). The interplanar distances between cores in the first−second layers and the second−third layers are 2.89 and 3.09 Å, respectively, and the shortest N···N distance is 3.08 Å. As shown in Figure 3g, one-dimensional pores with a triangular cross section with width of 8.8 Å are formed along the *c* axis. The wall of the channel has branched small spaces with diameter of ca. 3 Å. The ratio of total potential solvent area volume of **CPHATN-1a** was 20% (cell volume: 2989.6 Å^3, void volume per cell: 608.1 Å^3)

Structure Durability toward Common Solvents. To disclose structural durability of the framework toward common solvents, crystalline powder of **CPHATN-1a** was soaked in hot solvents [chloroform (333 K), toluene (373 K), ethanol (333 K), and water (373 K)] for 24 h. After being filtered, the samples were subjected to PXRD measurements. The original pattern of **CPHATN-1a** is retained for these solvents after filtration, and the peak intensity is recovered after the sample is heated to remove the solvent (Figure 4). Furthermore, it is remarkable that **CPHATN-1a** was regenerated even after being soaked in strong acid: although the PXRD pattern of the HCl-soaked sample is decayed significantly, the original pattern is recovered after removal of HCl by heating.

Evaluation of Permanent Porosity. The permanent porosity of **CPHATN-1a** was evaluated by nitrogen, oxygen, carbon dioxide, and hydrogen sorption measurements at 77, 77, 195, and 77 K, respectively (Figure S6). **CPHATN-1a** shows type-I sorption isotherms for all gases, indicating that it has micropores. The uptakes are 108.7 cm^3/g for N_2 at 99.7 kPa, 144 cm^3/g for O_2 at 20.9 kPa, 116.0 cm^3/g for CO_2 at 100.4 kPa, and 71.9 mL for H_2 at 101.7 kPa. The calculated BET surface area and pore size based on a N_2 sorption isotherm are 379 m^{2}g^{-1} and 0.78 nm, respectively (Figures S7 and S8).

To investigate precise structural changes upon sorption of hydrocarbons, PXRD patterns of **CPHATN-1a** were recorded upon introduction of vapors of benzene and hexane (Figure 5a,b). The 010 and 011 diffraction peaks are shifted into the small angle region upon vapor absorption, while the 001 peak remained at the original position. Furthermore, when the benzene-filled material **CPHATN-1(Ben)** is heated, the 010 and 011 peaks are shifted into the wide angle region, indicating shrinking of the cell due to a release of benzene molecules (Figure 5c). These structural changes consist of crystal structures of **CPHATN-1(TCB)** and **CPHATN-1a** (Figure 5d).

DOI: 10.1021/jacs.8b12124
J. Am. Chem. Soc. 2019, 141, 2111−2121

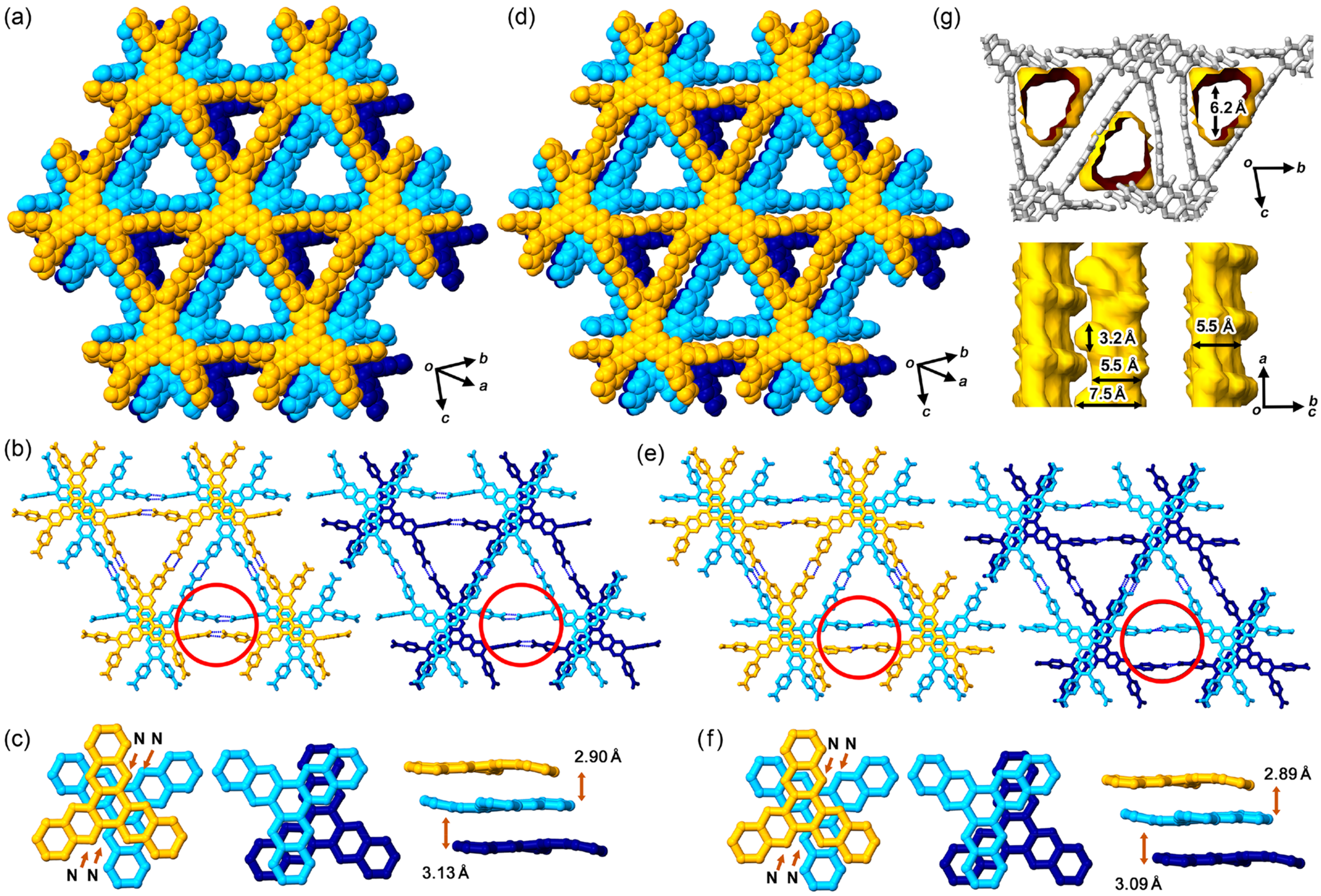

Figure 3. Crystal structures of solvate **CPHATN-1(TCB)** (a−c) and activated form **CPHATN-1a** (d−f). (a, d) Three layers of the stacked H-HexNet sheets, where first, second, and third layers are colored yellow, cyan, and blue, respectively. (b, e) Relative orientation of the stacked first−second and second−third layers (left and right, respectively). (c, f) Relative orientation of the stacked cores: first−second cores (left), second−third cores (middle), and side view of the stacking (right). (g) Visualized surface of the activated void in **CPHATN-1a** with the Mercury software. In the crystal structure of **CPHATN-1(TCB)**, solvent molecules (TCB) are accommodated in the voids but are severely disordered. Red circles in (b, e) refer to the conformationally frustrated carboxy dimers, which experience structural changes upon activation.

Table 1. Crystal Data of CPHATN-1(TCB) and CPHATN-1a

	CPHATN-1(TCB)	CPHATN-1a	difference
space group	*P*-1	*P*-1	
a (Å)	7.27754(17)	7.3893(4)	+0.111
b (Å)	20.8039(4)	19.3980(11)	−1.406
c (Å)	21.7135(4)	21.3787(10)	−0.335
α (deg)	76.5118(17)	80.108(4)	+3.60
β (deg)	89.6714(17)	88.822(4)	−0.85
γ (deg)	86.3993(18)	82.022(5)	−4.38
V (Å^3)	3190.33(12)	2989.6(3)	−200.73
void per cell (Å^3)	843.0	608.1	−234.9

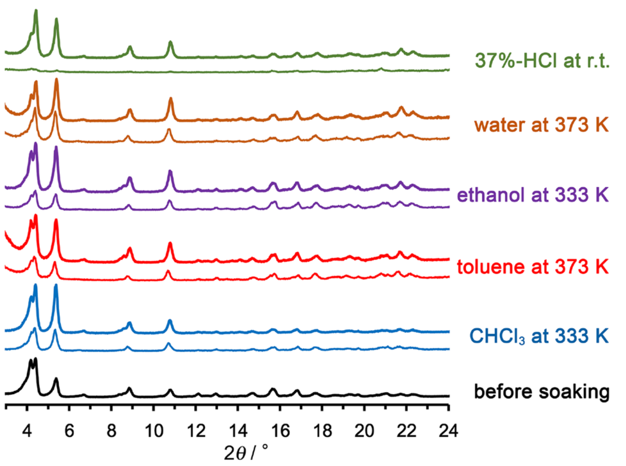

Figure 4. PXRD patterns of crystalline bulk of **CPHATN-1a** before and after soaking into hot solvents for 24 h. Thin lines: after filteration. Bold lines: after heating the filtered samples at 423 K for 1 h to remove the solvents.

Steady-State Absorption and Emission Studies. Figure 6a shows the absorption and emission spectra of **CPHATN-1a** in the solid state, which display intensity maxima at 447 and 539 nm, respectively. The shoulder at around 500 nm reflects the $S_0 \rightarrow S_1$ transition onset. The absorption band exhibits a large full-weigh at half-maximum (fwhm) of intensity (~27000 cm^{-1}), which probably reflects the existence of different absorbing species or strong spectral overlap of $S_0 \rightarrow S_1$ and $S_0 \rightarrow S_2$ bands. Recently, we have reported on the photobehavior of **CPHAT** and **CBPHAT** materials, which have similar fundamental units.[10] The difference between these materials and the one here studied is the presence of an extra benzene ring joined to each pyrazine group (Figure 1). Comparing their UV−vis absorption spectra, we observe a large bathochromic shift of **CPHATN-1a** one (447 nm) with respect to those of

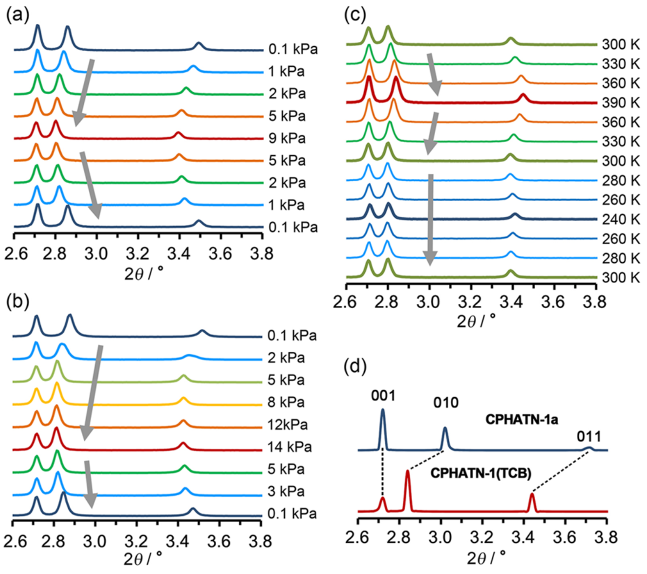

Figure 5. PXRD pattern changes of **CPHATN-1a** upon sorption of (a) benzene and (b) hexane vapor. (c) VT-PXRD patterns of benzene-filled material **CPHATN-1(Ben)**. (d) Simulated patterns of **CPHATN-1(TCB)** and **CPHATN-1a**. The diffraction patterns were recorded with synchrotron X-ray radiation with wavelength of 1.000 Å at BL02B2 in SPring-8.[25]

CPHAT (392 nm) and **CBPHAT** (404 nm). This reflects a larger π-conjugation in the molecular frame of **CPHATN-1a** produced due to the core by the addition of the three extra benzene groups, as it has been observed in other studied molecules.[26]

The emission spectrum of **CPHATN-1a** has an intensity maximum at 539 nm and displays a large red-shifted band in comparison with those of **CPHAT** (470 nm) and **CBPHAT** (491 nm) ones. The shift is explained by an increment in the π-conjugation in the core of the fundamental units of the material. Moreover, the fwhm of **CPHATN-1a** emission band is ~1900 cm^{-1}, smaller than those of **CPHAT-1a** (3300 cm^{-1}) and **CBPHAT-1a** (2900 cm^{-1}).

The fluorescence excitation spectra of **CPHATN-1a** do not depend on the observation wavelength but display different spectral shapes when compared to that of the absorption one (Figures 6a and S9). Furthermore, they exhibit intensity maxima at 370 and 504 nm. The different shapes of the excitation spectra suggest the opening of efficient no-radiative channels when excited at wavelengths between 400 and 500 nm. Based on the structure of the fundamental units, we consider that the unpaired electrons of the six nitrogen atoms, which form the core, make more efficient the nonradiative channels due to the coupling with the (n,π*) states.[10] The shape and peaks positions in the excitation spectra also suggest that the absorption at 370 and 504 nm are due to the $S_0 \rightarrow S_2$ and $S_0 \rightarrow S_1$ transitions, respectively.

Picosecond Time-Resolved Experiments. To elucidate the behavior of the excited species in the crystals, we carried out picosecond time-resolved emission experiments[27] on **CPHATN-1a** (Figure 6b). The decays exhibit a multi-exponential behavior with time constants of 190 and 507 ps and 2.51 ns. All of the components are decaying along the whole observation range. The contribution of the fastest component (190 ps) in the emission decay decreases at longer wavelengths, while that of the slowest one (2.51 ns) appears from 550 nm (the intensity maximum of the steady-state spectrum) (Table 2). We suggest that the shortest component corresponds to the emission from the initially excited species, while that of the slowest decay reflects emitting structures formed after an ultrafast event in the formers. We believe that this photoinduced process is an intermolecular proton-transfer between two acid groups of the fundamental units in the crystals (Figure 1). It is worth mentioning that the time-

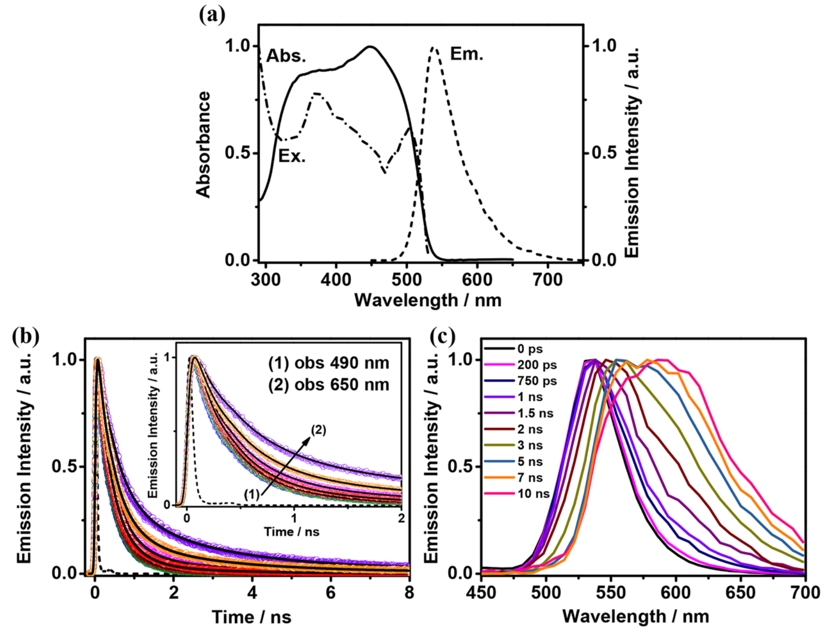

Figure 6. (a) (Solid line) UV–visible absorption, (dashed line) emission, and (dash dot) excitation spectra of the crystals ensemble of **CPHATN-1a**. The excitation wavelength was 370 nm. (b) Magic-angle emission decays of the solid of **CPHATN-1a**, upon excitation at 371 nm, and recording at the indicated wavelengths. The solid lines are from the best global fit using a multiexponential function. (c) Normalized time-resolved emission-spectra (TRES) of the ensemble solid of **CPHATN-1a**. The excitation wavelength was 371 nm and gating at the indicated delay times.

DOI: 10.1021/jacs.8b12124
J. Am. Chem. Soc. 2019, 141, 2111–2121

Table 2. Values of Time Constants (τ_i), Normalized (to 100) Pre-exponential Factors (A_i), and Contributions ($c_i = \tau_i \times A_i$) Obtained from a Global Multiexponential Fit of the Emission Decays of the Ensemble Solid of CPHATN-1a upon Excitation at 371 nm and Observation As Indicated

sample	λ_{obs} (nm)	τ_1 (ps) ± 30 ps	A_1	c_1	τ_2 (ps) ± 50 ps	A_2	c_2	τ_3 (ns) ± 0.2 ns	A_3	c_3
ensemble solid of **CPHATN-1a**	490	190	59	35	507	41	65			
	510		55	33		45	67			
	530		54	32		46	68			
	540		54	32		45	61	2.51	1	7
	550		53	28		45	62		2	10
	570		48	23		48	57		4	20
	590		42	15		51	50		7	35
	610		32	9		54	40		14	51
	650		20	4		54	28		26	68

resolution of the setup (~20 ps) does not allow us to obtain an accurate time constant for the process. We will discuss the ultrafast events in the femtosecond part. However, to support the above assignment, we have to take into account the H-bond interactions between the acid groups and the $\pi-\pi$ stacking between the core units. For **T12-apo** (HOF), we have previously reported the presence of two different kind of crystals, whose photobehavior is conditioned by the main acting force in the crystal formation and stability.[26d] We found that the value of the fluorescence lifetime of excited **T12-apo** crystals is 20 ns when the main force between the core units forming the crystals interactions is due to $\pi-\pi$ stacking, and 8.5 ns for the H-bond stacking. While the **T12-apo** core does not contain nitrogen atoms, allowing $\pi-\pi$ stacking between their units; **CPHATN-1a**, which has six nitrogens in its core, will have difficulties packing by $\pi-\pi$ interactions due to the repulsion forces between the no-bonding orbitals of the nitrogen atoms. Therefore, the main signal of emission will be from crystals formed by the H-bonds interactions, contrary to those of $\pi-\pi$ stacking.

We assign the intermediate component (507 ps) to the emission of species produced after an intramolecular charge transfer (ICT) from the phenyl groups to the main core. **T12-apo** HOF undergoes an ICT event, and the time of the emitting species is ~5 ns.[10a,26c] The lifetimes of **CPHATN-1a** (190 and 507 ps and 2.51 ns) are much shorter than those of **T12-apo** (~1, ~5, ~8 ns). This difference is due to the presence of unpaired electrons on the nitrogen atoms in the **CPHATN-1a** core, opening a nonradiative coupling with not fluorescent (n, π^*) states, making faster the emission decays. It also explains the shape of the excitation spectra at shorter absorption wavelengths.

To obtain more information on the excited-state photobehavior, we recorded picosecond time-resolved emission spectra (TRES). Figures 6c and S10 show the normalized and not normalized TRES of the ensemble solid of **CPHATN-1a**. To begin with, with gating at times shorter than 300 ps, the spectra have their intensity maxima at ~538 nm with a fwhm of 1800 cm^{-1}, which is very close in value to that of the steady-state spectrum (1900 cm^{-1}), suggesting that the species at longer times exhibits a very lower fluorescence quantum yield. The TRES gated at longer times (≥400 ps) clearly show a red shift in their intensity maxima, and at 10 ns gating time, the intensity maximum is at 590 nm. In addition to that, the spectra become wider (fwhm = 3200 cm^{-1}), reflecting the emission from different species. Moreover, the Stock shift between the intensity maximum of the excitation spectrum (504 nm from the $S_0 \rightarrow S_1$ transition) and the maximum of the TRES at longer gating times is large (2900 cm^{-1}), suggesting that an intermolecular proton-transfer is occurring at the excited state, as we comment before.

The excitation spectrum displays two bands (Figure 6a), and we recorded spectra at other wavelengths (433 and 470 nm) to explore the nature of these bands. Figure S10 exhibits the emission decays up both excitations, while Table S3 gives the obtained values from the best fits. The difference in the lifetime values, using three excitation wavelengths, is within the expected error from the experiments and fits, indicating that the emitting species are very similar. However, comparing the contribution of the shortest component at the bluest part of the emission band, we observe an increase from 55% (exciting at 371 nm) to 75% when the excitation shifts from 371 to 470 nm. As we said above, this component reflects the emission from the initially excited state. After excitation, few of these species may exhibit an ICT process. Therefore, when we pump with a lower energy (470 nm), some structures may not undergo the ICT event, and the emission intensity from the initially pumped state increases. However, when we excite with more excess energy (370 nm), a larger population of these species could undergo the ICT reaction, which is reflected by a decrease in the contribution of the shortest component. This behavior indicates the presence of an energy barrier between the potential-energy surfaces of the initially excited structures and the formed ICT species.

Femtosecond Time-Resolved Experiments. To explore the ultrafast processes, we carried out femtosecond (fs) experiments on **CPHATN-1a** in the solid state. We excited at 400 nm and gated the emission at different wavelengths. Figure 7 shows the fs emission transients decays in a short time window, while Figure S12 displays the complete decays. Using a multiexponential model to fit the emission decays, we obtained three time constants with values of 1.1, 20, and 190 ps, with the longest one a fixed value in the fit, and using that of the picosecond data (Table 3). The shortest component is decay at the bluest part and becomes a rise from 540 nm, while the other ones decay over the all-emission spectrum. Note also that the up-conversion signals at 470−520 show an ultrafast rise, which is under the time resolution of the setup (~100 fs). Taking into account the spectral position of the ultrafast (≤100 fs) and fast (1.1 ps) components, we suggest the following assignments, in agreement with that already discussed in the ps-part. The ultrafast rising component at the bluest emission region reflects the ICT reaction, while the 1.1 ps value (decay and rise) is due to intermolecular proton transfer between the acid groups of the fundamental units of the crystals. The 20 ps component most probably originates

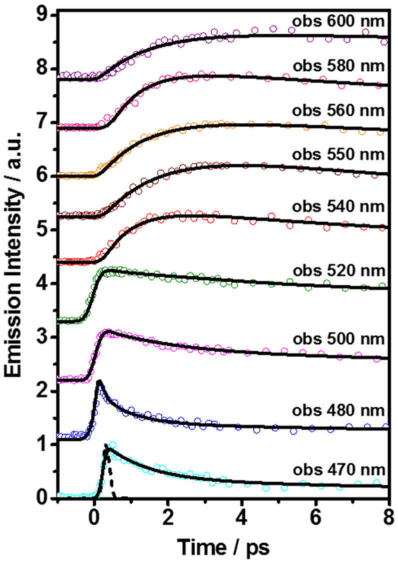

Figure 7. Representative femtosecond emission transients of **CPHATN-1a** in the solid state upon excitation at 400 nm. The observation wavelengths are indicated in the inset. The solid lines are from the best fit using a multiexponential function, and the dash line denotes the instrumental response function (IRF).

Table 3. Values of Time Constants (τ_i) and Normalized (to 100) Pre-exponential Factors (A_i) Obtained from the Best Fit of the Femtosecond Emission Decays of the Ensemble Solid of CPHATN-1a upon Excitation at 400 nm and Observation As Indicated

sample	λ_{obs} (nm)	τ_1 (ps)	A_1	τ_2 (ps)	A_2	τ_3 (ps)[a]	A_3
ensemble solid of **CPHATN-1a**	470	1.1	80	18	10	190[a]	10
	480	1.1	79	20	11		10
	500	1.2	43	22	45		12
	520	1.2	17	22	63		20
	540	0.8	−100	18	78		22
	550	1.0	−100	18	72		28
	560	1.2	−100	21	70		30
	580	1.1	−100	20	73		27
	600	1.2	−100	22	28		72

[a] The negative sign of A_i indicates a rising component in the emission signal.

from structures having suffered a fast crossing to the dark (n,π*) states, as previously mentioned. Moreover, it is well-known that these kinds of materials (HOFs, MOFs and COFs) are not free from defects, which can change their photophysical properties.[28] Defects can also be very beneficial for LED and photocatalysis applications.[29] These defects enhance non-radiative transitions. In the following part, we examine the emission lifetime and spectra at single and several crystals for obtaining further knowledge on the effect of defects on their photobehavior.

Confocal Microscopy Fluorescence and Time-Resolved Studies. To elucidate the effect of the size, cracking, and possible defects on the photodynamics, we performed confocal fluorescence microscopy studies of single crystals. Figure 8a shows the fluorescence image (FLIM) of a representative single crystal of around 35 μm in length. Figure 8b displays the emission spectra at different selected points of the crystal. Interestingly, we observed a spectral red-shift between the points 1−3 and 4−9. It turns out that points 1−3 are on the cracks and borders of the signal crystal (Figure 8a). This behavior has been also observed on a similar HOF.[10b] As noted above, these kinds of materials are not free from defects, which can change their photophysical properties. Furthermore, we performed the same experiments on crystals of different sizes and forms (Figure 9a,b and Figures S13a,b and S14a,b). The emission spectra show a small red-shift, as we observed for the single crystal.

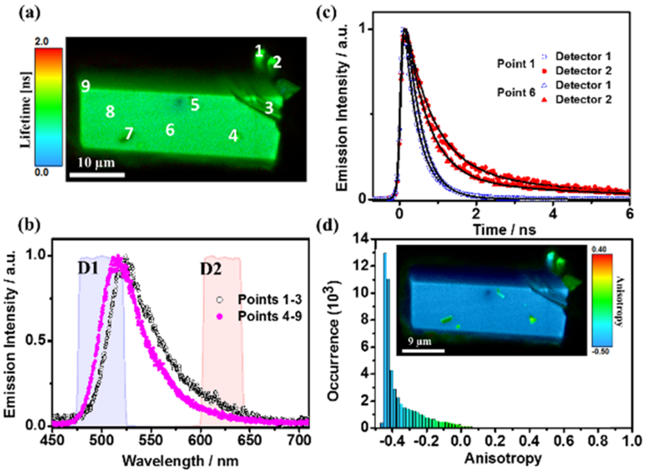

Figure 8. (a) Fluorescence image of a single **CPHATN-1a** crystal. (b) Emission spectra at different points of the related crystal. (c) Emission decays at selected spectral range using two different filters of transmission to gate at D1 or at D2 region as shown in (b). For detector 1 (D1), we used a FF01-625-32-25 Chroma filter, and for detector 2 (D2), we used a FF01-503-40-25 Chroma filter. The solid lines are from the best-fit using a multiexponential function. (d) Histogram of the emission anisotropy for the related crystal. The excitation wavelength was 390 nm.

We also collected the picosecond emission decays at the same positions for the emission spectra, although we only show representative ones (Figures 8c, 9c, and S12c and S13c). The decays were recorded at two different regions of the emission spectrum using two detectors: detector 1 (D1) for the blue-green emission region (475−525 nm) and detector 2 (D2) for the red one (600−650 nm). Table 4 shows a summary of the obtained results using a multiexponential fit of the decays, while Table S4 gives the obtained lifetimes and pre-exponential values. Interestingly, by gating at the blue-green region (D1), we obtained time values of 220−400 ps and 0.5−0.6 ns, while recording at the red region (D2) we got 500−700 ps and 2.7−3.7 ns. These values are comparable to 190 ps, 507 ps, and 2.71 ns lifetimes obtained from the ps experiments on the ensemble. Therefore, the shortest component comes from the initially excited state, while the 500−700 ps is attributed to species having suffered an ICT process. Finally, the longest lifetime (2.7−3.7 ns) is assigned to the species formed after an intermolecular proton-transfer reaction in the crystal.

To this end, fluorescence confocal microcopy measurements on **CPHATN-1a** crystals show high anisotropic emission behavior (Figure 8d). The anisotropy displays a value of −0.44, which corresponds to a parallel orientation to the observation plane. Moreover, there is a low population, which exhibits an anisotropy centered at −0.2. Taking into account the anisotropy image, we observe that the large and main crystal displays the more negative value, while the smallest ones adsorbed on the surface of the main crystal, and also the

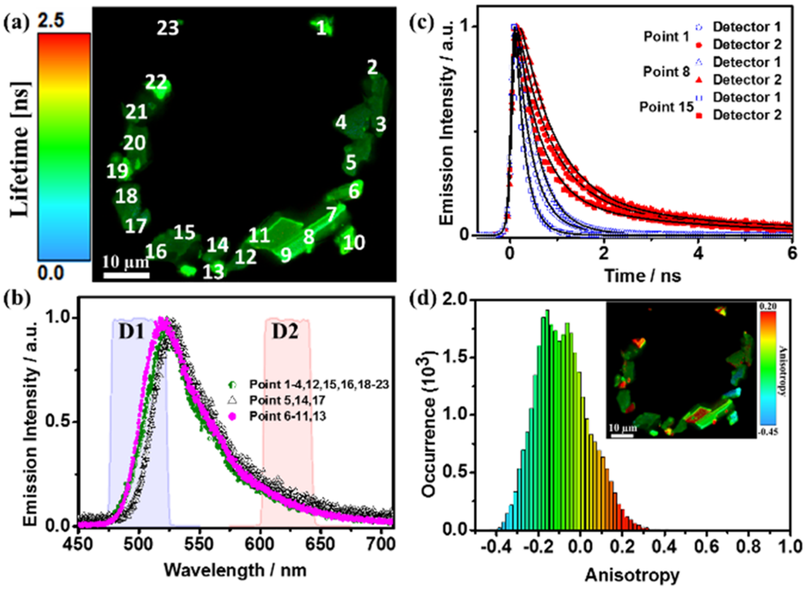

Figure 9. (a) FLIM of **CPHATN-1a** crystals. (b) Emission spectra at different points of the crystals. (c) Emission decays at selected spectral range using two different filters (D1 and D2 in (b)). The solid lines are from the best-fit using a multiexponential function. (d) Histogram of the emission anisotropy for the shown FLIM. The excitation wavelength was 390 nm.

Table 4. Summary of the Values of Time Constants (τ_i) and Normalized (to 100) Pre-exponential Factors (A_i) Obtained from the Fit of the Emission Decays of the Different Points of the Different Point and Crystals of CPHATN-1a

image of Figure	detector	τ_1 (ps) ± 50 ps	A_1	τ_2 (ns) ± 0.2 ns	A_2
8	1	220–300	96–98	0.5–0.6	4–2
	2	540–600	84–90	2.7–3.0	16–10
9	1	240–300	96–98	0.5–0.6	4–2
	2	500–600	84–91	2.7–3.0	16–9
S13	1	280–310	96–98	0.5–0.6	6–2
	2	600–660	82–90	2.9–3.0	18–10
S14	1	300–400	96–98	0.6–0.7	4–2
	2	600–700	82–94	3.2–3.7	18–6

defects of the main crystal display other values, which form the tail of the anisotropy. The different values reflect the different disposition of the crystals. Similar behavior has been found for **CPHAT-1a** and **CBPHAT-1a.**[10] Therefore, the anisotropic behavior suggests that the crystalline structure of **CPHATN-1a** has a preferential orientation of the molecular dipole moments perpendicular to the long axis with the $\pi-\pi$ stacking. This fact is also supported by the results from other crystals. For example, Figure 8d presents the anisotropy histogram of several crystals. The histogram is large, clearly reflecting the different orientations of the crystals. Furthermore, Figure S13d shows the result of another large crystal. The histogram shows two maxima at −0.1 and +0.67 and a shoulder at 0.46. The highest occurrence corresponds to the large crystal which is vertically oriented, contrary to one of a negative anisotropy (−0.44), having a horizontal orientation (Figure 8d).

Acid-Induced Color Changes. It is remarkable that **CPHATN-1a** shows color changes by exposing it to HCl. As shown in Figure 10a, yellow crystalline bulks of **CPHATN-1a** immediately turned into redish-brown by adding a drop of 37% HCl aqueous solution. Subsequence heating of the brown bulks resulted into recovery of the original yellow color due to removal of HCl. Note that the acid-responsive color change was also observed in the case of crystalline solvate **CPHATN-1(TCB)**, while is not observed in a solution state of **CPHATN** (Figures S15−S17). This characteristic color changes observed only for the solid state suggests that the color changes might be brought about not only by protonation of the HATN core but by intermolecular interactions among protonated and neutral HATN cores.

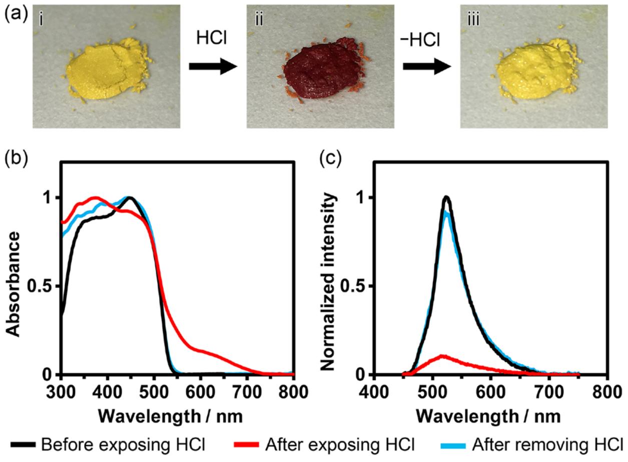

Figure 10. (a) HCl-responsive color changes of crystalline bulks of **CPHATN-1a** (i) before exposure, (ii) after 37%-HCl was dropped on, and (iii) after heating at 423 K for 30 min. (b) Absorption and (c) emission spectra of solid **CPHATN-1a** upon exposure to HCl atmosphere for 40 min and after leaving the exposed crystals in air during 48 h to remove HCl.

To obtain structural information on **CPHATN-1a** upon HCl exposing, PXRD pattern of the crystalline bulks were recorded before exposure, after adding a drop of 37% HCl, and after heating at 423 K for 30 min (Figure S18). The PXRD patterns were once disappeared by adding a HCl drop, while the original pattern was completely recovered after heating the HCl-dropped sample. This tendency is the same as that for the HCl soaked sample (Figure 4). The disappearance of the PXRD patterns is presumably attributed to (1) disorder of the framework by adding HCl and/or (2) scattering of diffracted X-ray by disordered Cl^- and H_3O^+ ions filling the void. To exclude the second factor and estimate the only effects of HCl, **CPHATN-1a** was exposed to a vapor of HCl. Color was changed upon exposre to HCl vapor (Figure S19), and simultaneously, new peaks at 4.86, 5.78, 9.78, and 11.7° appeared in PXRD patterns in addition to the original peaks (Figure S20). The new peaks disappear when the sample is heated to remove HCl and back to the orignal yellow solid. These results indicate that addition of HCl and protonation of the HATN core perturbs the structure of the original framework, resulting changes and decay of PXRD patterns.

When the HOF crystals are exposed to HCl vapors, the absorption and emission spectra show insignificant changes (Figure 10b). The absorption spectrum exhibits a new band at 500−600 nm, while the emission spectrum is strongly quenched. These observations clearly indicate the sensitivity of this HOF to acid vapors, and are explained in terms of strong interactions of the protons acid with the core of the fundamental unit, as we said above. Interestingly, the original absorption and emission spectra are ∼90% recovered by clearing the HOF crystals in air and at ambient temperature during 48 h (Figure 10b). Thus, we can use this HOF as sensor of acid atmospheres for several times. Furthermore, we recorded ps-emission decays of the HOF exposed to HCl vapor (Figure S21). We excited at 470 nm where the protoned crystals absorbs. The decays show a multiexponential behavior with time constants of 73 ps, 360 ps and 1.81 ns (Table S5). All of the components decay over the entire spectral range, and while the contribution of the shortest component decreases in the red part, the others two increase. The time constants are shorter than those of the original HOF (190, 507 ps and 2.51 ns), in agreement with the strong quenching observed in the emission spectrum. Because 470 nm excitation will also pump a population of unprotonated HOF, the recorded decays should be a combination of protonated and unprotonated crystals.

■ CONCLUSION

In this work, we demonstrated for the first time that hexaazatrinaphthylene derivatives with carboxy phenyl groups (**CPHATN**) can be a suitable building block to construct acid-responsive porous crystalline materials. Facile recrystallization of **CPHATN** solution gave a hydrogen-bonded organic framework (HOF) with a layered structure of a hexagonal network. Precise structures of both 1,2,4-trichlorobenzene solvate [**CPHATN-1(TCB)**] and activated HOF with permanent porosity (**CPHATN-1a**) were successfully determined by single-crystalline X-ray diffraction analysis. Permanent porosity of **CPHATN-1a** is evaluated by gas sorption experiments at low temperature. Thermal stability of **CPHATN-1a** is also evaluated by VT-PXRD, disclosing its stability up to at least 633 K. fs−ps time-resolved emission experiments indicate the occurrence of an ICT (≤200 fs) and intermolecular proton trasnfer (1.2 ps) reactions in the HOF. Single-crystal fluoroescence microscopy reveals the high orientation of the units to form the crystals and shows the importance of defects and cracking in their photobehavior. Remarkably, **CPHATN-1a** exhibits reversible acid-induced color changes and ON/OFF of its emission due to protonation/deprotonation of the pyridyl nitrogen atoms embedded in its π-conjugated core. Thus, we believe that the present system provides new insights for developing stimuli-responsive HOFs.

■ ASSOCIATED CONTENT

Supporting Information

The Supporting Information is available free of charge on the ACS Publications website at DOI: 10.1021/jacs.8b12124.

Details of synthesis and characterization, photophysical properties, and photographs for color changes of the HOF (PDF)

X-ray data for **CPHATN-1(TCB)** (CIF)

X-ray data for **CPHATN-1a** (CIF)

X-ray data for **CPHATN-NP(DMAc)** (CIF)

X-ray data for **CPHATN-NP(NMP)** (CIF)

■ AUTHOR INFORMATION

Corresponding Authors

*hisaki@es.hokudai.ac.jp
*abderrazzak.douhal@uclm.es

ORCID

Ichiro Hisaki: 0000-0002-8170-5605
Eduardo Gomez: 0000-0002-0079-7852
Norimitsu Tohnai: 0000-0001-7051-7599
Abderrazzak Douhal: 0000-0003-2247-7566

Author Contributions

[∥]Y.S. and E.G. contributed equally.

Notes

The authors declare no competing financial interest.
Crystallographic data (1877479−1877481 and 1886521) have been submitted to The Cambridge Crystallographic Data Centre.

■ ACKNOWLEDGMENTS

This work is supported by a Grant-in-Aid for Scientific Research (C) (JP15K04591 to I.H.) and (B) (JP18H01966 to I.H.) from MEXT Japan and by the MINECO through projects MAT2014-57646-P and MAT2017-86532-R to A.D. E.G. thanks the MINECO for a Ph.D. fellowship: FPU15/01362. X-ray diffraction experiments were partly conducted at BL38B1 and BL02B2 in SPring-8 with approval of JASRI (Proposal Nos. 2017B1322, 2018A1327, 2017B1325, and 2018A1238). The authors thank Dr. S. Kawaguchi (JASRI/SPring-8) for PXRD measurements under gas absorption−desorption conditions.

■ REFERENCES

(1) (a) Slater, A. G.; Cooper, A. I. Functionled design of new porous materials. *Science* **2015**, *348*, aaa8075. (b) Das, S.; Heasman, P.; Ben, T.; Qiu, S. Porous organic materials: strategic design and structure-function correlation. *Chem. Rev.* **2017**, *117*, 1515.

(2) Côté, A. P.; Benin, A. I.; Ockwig, N. W.; O'Keeffe, M.; Matzger, A. J.; Yaghi, O. M. Porous, crystalline, covalent organic frameworks. *Science* **2005**, *310*, 1166.

(3) (a) Feng, X.; Ding, X.; Jiang, D. Covalent organic frameworks. *Chem. Soc. Rev.* **2012**, *41*, 6010. (b) Ding, S.-Y.; Wang, W. Covalent organic frameworks (COFs): from design to applications. *Chem. Soc. Rev.* **2013**, *42*, 548. (c) Dogru, M.; Bein, T. On the road towards electroactive covalent organic frameworks. *Chem. Commun.* **2014**, *50*, 5531. (d) Waller, P. J.; Gandara, F.; Yaghi, O. M. Chemistry of covalent organic frameworks. *Acc. Chem. Res.* **2015**, *48*, 3053. (e) Zhao, W.; Xia, L.; Liu, X. Covalent organic frameworks

(COFs): perspectives of industrialization. *CrystEngComm* **2018**, *20*, 1613.

(4) (a) Luo, J.; Wang, J.-W.; Zhang, J.-H.; Lai, S.; Zhong, D.-C. Hydrogen-bonded organic frameworks: design, structures and potential applications. *CrystEngComm* **2018**, *20*, 5884. (b) Lu, J.; Cao, R. Porous organic molecular frameworks with extrinsic porosity: a platform for carbon storage and separation. *Angew. Chem., Int. Ed.* **2016**, *55*, 9474.

(5) (a) For examples, see: Yang, W.; Greenaway, A.; Lin, X.; Matsuda, R.; Blake, A. J.; Wilson, C.; Lewis, W.; Hubberstey, P.; Kitagawa, S.; Champness, N. R.; Schröder, M. A robust binary supramolecular organic framework (SOF) with high CO_2 adsorption and selectivity. *J. Am. Chem. Soc.* **2010**, *132*, 14457. (b) Tian, J.; Zhou, T.-Y.; Zhang, S.-C.; Aloni, S.; Altoe, M. V.; Xie, S.-H.; Wang, H.; Zhang, D.-W.; Zhao, X.; Liu, Y.; Li, Z.-T. Three-dimensional periodic supramolecular organic framework ion sponge in water and microcrystals. *Nat. Commun.* **2014**, *5*, 5574.

(6) (a) Yin, Q.; Zhao, P.; Sa, R.-J.; Chen, G.-C.; Lü, J.; Liu, T.-F.; Cao, R. An ultra-robust and crystalline redeemable hydrogen-bonded organic framework for synergistic chemo-photodynamic therapy. *Angew. Chem., Int. Ed.* **2018**, *57*, 7691. (b) Yamagishi, H.; Sato, H.; Hori, A.; Sato, Y.; Matsuda, R.; Kato, K.; Aida, T. Self-assembly of lattices with high structural complexity from a geometrically simple molecule. *Science* **2018**, *361*, 1242.

(7) (a) He, Y.; Xiang, S.; Chen, B. A microporous hydrogen-bonded organic framework for highly selective C_2H_2/C_2H_4 separation at ambient temperature. *J. Am. Chem. Soc.* **2011**, *133*, 14570. (b) Wang, H.; Li, B.; Wu, H.; Hu, T.-L.; Yao, Z.; Zhou, W.; Xiang, S.; Chen, B. A flexible microporous hydrogen-bonded organic framework for gas sorption and separation. *J. Am. Chem. Soc.* **2015**, *137*, 9963. (c) Hisaki, I.; Nakagawa, S.; Suzuki, Y.; Tohnai, N. CO_2 Sorption of layered hydrogen-bonded organic framework causes reversible structural changes involving four different crystalline states under ambient pressure. *Chem. Lett.* **2018**, *47*, 1143.

(8) (a) Maly, K. E.; Gagnon, E.; Maris, T.; Wuest, J. D. Engineering hydrogen-bonded molecular crystals built from derivatives of hexaphenylbenzene and related compounds. *J. Am. Chem. Soc.* **2007**, *129*, 4306. (b) Yang, J.; Dewal, M. B.; Profeta, S.; Smith, M. D., Jr.; Li, Y.; Shimizu, L. S. Origins of selectivity for the [2 + 2] cycloaddition of α,β-unsaturated ketones within a porous self-assembled organic Framework. *J. Am. Chem. Soc.* **2008**, *130*, 612. (c) Comotti, A.; Bracco, S.; Distefano, G.; Sozzani, P. Methane, carbon dioxide and hydrogen storage in nanoporous dipeptide-based materials. *Chem. Commun.* **2009**, 284. (d) Mastalerz, M.; Oppel, I. Rational construction of an extrinsic porous molecular crystal with an extraordinary high specific surface area. *Angew. Chem., Int. Ed.* **2012**, *51*, 5252. (e) Luo, X.-Z.; Jia, X.-J.; Deng, J.-H.; Zhong, J.-L.; Liu, H.-J.; Wang, K.-J.; Zhong, D.-C. A microporous hydrogen-bonded organic framework: exceptional stability and highly selective adsorption of gas and liquid. *J. Am. Chem. Soc.* **2013**, *135*, 11684. (f) Lü, J.; Perez-Krap, C.; Suyetin, M.; Alsmail, N. H.; Yan, Y.; Yang, S.; Lewis, W.; Bichoutskaia, E.; Tang, C. C.; Blake, A. J.; Cao, R.; Schröder, M. A robust binary supramolecular organic framework (SOF) with high CO_2 adsorption and selectivity. *J. Am. Chem. Soc.* **2014**, *136*, 12828. (g) Comotti, A.; Bracco, S.; Yamamoto, A.; Beretta, M.; Hirukawa, T.; Tohnai, N.; Miyata, M.; Sozzani, P. Engineering switchable rotors in molecular crystals with open porosity. *J. Am. Chem. Soc.* **2014**, *136*, 618. (h) Chen, T.-H.; Popov, I.; Kaveevivitchai, W.; Chuang, Y.-C.; Chen, Y.-S.; Daugulis, O.; Jacobson, A. J.; Miljanić, O. Š. Thermally robust and porous noncovalent organic framework with high affinity for fluorocarbons and CFCs. *Nat. Commun.* **2014**, *5*, 5131. (i) Li, P.; He, Y.; Zhao, Y.; Weng, L.; Wang, H.; Krishna, R.; Wu, H.; Zhou, W.; O'Keeffe, M.; Han, Y.; Chen, B. A rod-packing microporous hydrogen-bonded organic framework for highly selective separation of C_2H_2/CO_2 at room temperature. *Angew. Chem., Int. Ed.* **2014**, *54*, 574. (j) Yadav, V. N.; Comotti, A.; Sozzani, P.; Bracco, S.; Bonge-Hansen, T.; Hennum, M.; Görbitz, C. H. Microporous molecular materials from dipeptides containing non-proteinogenic sesidues. *Angew. Chem., Int. Ed.* **2015**, *54*, 15684. (k) Zentner, C. A.; Lai, H. W. H.; Greenfield, J. T.; Wiscons, R. A.; Zeller, M.; Campana, C. F.; Talu, O.; FitzGerald, S. A.; Rowsell, J. L. C. High surface area and Z' in a thermally stable 8-fold polycatenated hydrogen-bonded framework. *Chem. Commun.* **2015**, *51*, 11642. (l) Nandi, S.; Chakraborty, D.; Vaidhyanathan, R. A permanently porous single molecule H-bonded organic framework for selective CO_2 capture. *Chem. Commun.* **2016**, *52*, 7249. (m) Yang, W.; Wang, J.; Wang, H.; Bao, Z.; Zhao, J. C.-G.; Chen, B. Highly Interpenetrated Robust Microporous Hydrogen-Bonded Organic Framework for Gas Separation. *Cryst. Growth Des.* **2017**, *17*, 6132. (n) Hu, F.; Liu, C.; Wu, M.; Pang, J.; Jiang, F.; Yuan, D.; Hong, M. An ultrastable and easily regenerated hydrogen-bonded organic Mmolecular framework with permanent porosity. *Angew. Chem., Int. Ed.* **2017**, *56*, 2101. (o) Hashim, M. I.; Le, H. T. M.; Chen, T.-H.; Chen, Y.-S.; Daugulis, O.; Hsu, C.-W.; Jacobson, A. J.; Kaveevivitchai, W.; Liang, X.; Makarenko, T.; Miljanić, O. Š.; Popovs, I.; Tran, H. V.; Wang, X.; Wu, C.-H.; Wu, J. I. Dissecting porosity in molecular crystals: influence of geometry, hydrogen bonding, and $[\pi\cdots\pi]$ stacking on the solid-state packing of fluorinated aromatics. *J. Am. Chem. Soc.* **2018**, *140*, 6014.

(9) (a) Hisaki, I.; Nakagawa, S.; Tohnai, N.; Miyata, M. A C_3-symmetric macrocycle-based, hydrogen-bonded, multiporous hexagonal network as a motif of porous molecular crystals. *Angew. Chem., Int. Ed.* **2015**, *54*, 3008. (b) Hisaki, I.; Ikenaka, N.; Tohnai, N.; Miyata, M. Polymorphs of layered assemblies of hydrogen-bonded hexagonal networks caused by conformational frustration. *Chem. Commun.* **2016**, *52*, 300. (c) Hisaki, I.; Nakagawa, S.; Ikenaka, N.; Imamura, Y.; Katouda, M.; Tashiro, M.; Tsuchida, H.; Ogoshi, T.; Sato, H.; Tohnai, N.; Miyata, M. A series of layered assemblies of hydrogen-bonded, hexagonal networks of C_3-symmetric π-conjugated molecules: a potential motif of porous organic materials. *J. Am. Chem. Soc.* **2016**, *138*, 6617. (d) Hisaki, I.; Nakagawa, S.; Sato, H.; Tohnai, N. Alignment of paired molecules of C_{60} within a hexagonal platform networked through hydrogen-bonds. *Chem. Commun.* **2016**, *52*, 9781. (e) Hisaki, I.; Affendy, N. Q. E.; Tohnai, N. Precise elucidations of stacking manners of hydrogen-bonded two-dimensional organic frameworks composed of X-shaped π-conjugated systems. *CrystEngComm* **2017**, *19*, 4892. (f) Hisaki, I.; Toda, H.; Sato, H.; Tohnai, N.; Sakurai, H. A hydrogen-bonded hexagonal buckybowl framework. *Angew. Chem., Int. Ed.* **2017**, *56*, 15294. (g) Hisaki, I.; Ikenaka, N.; Tsuzuki, S.; Tohnai, N. Sterically crowded hydrogen-bonded hexagonal network frameworks. *Mater. Chem. Front.* **2018**, *2*, 338.

(10) (a) Hisaki, I.; Ikenaka, N.; Gomez, E.; Cohen, B.; Tohnai, N.; Douhal, A. Hexaazatriphenylene-based hydrogen-bonded organic framework with permanent porosity and single-crystallinity. *Chem. - Eur. J.* **2017**, *23*, 11611. (b) Hisaki, I.; Suzuki, Y.; Gomez, E.; Cohen, B.; Tohnai, N.; Douhal, A. Docking strategy to construct thermostable, single-crystalline, hydrogen-bonded organic framework with high surface area. *Angew. Chem., Int. Ed.* **2018**, *57*, 12650.

(11) For a review, see: Segura, J. L.; Juárez, R.; Ramos, M.; Seoane, C. Hexaazatriphenylene (HAT) derivatives: from synthesis to molecular design, self-organization and device applications. *Chem. Soc. Rev.* **2015**, *44*, 6850.

(12) Skujins, S.; Webb, G. A. Spectroscopic and structural studies of some oxocarbon condensation products—I: Preparation and characterization of some substituted phenazines and quinoxalines. *Tetrahedron* **1969**, *25*, 3935.

(13) (a) Crispin, X.; Cornil, J.; Friedlein, R.; Okudaira, K. K.; Lemaur, V.; Crispin, A.; Kestemont, G.; Lehmann, M.; Fahlman, M.; Lazzaroni, R.; Geerts, Y.; Wendin, G.; Ueno, N.; Brédas, J.-L.; Salaneck, R. Electronic delocalization in discotic liquid crystals: a joint experimental and theoretical study. *J. Am. Chem. Soc.* **2004**, *126*, 11889. (b) Lehmann, M.; Kestemont, G.; Aspe, R. G.; Buess-Herman, C.; Koch, M. H. J.; Debije, M. G.; Piris, J.; Haas, M. P., de; Warman, J. M.; Watson, M. D.; Lemaur, V.; Cornil, J.; Geerts, Y. H.; Gearba, R.; Ivanov, D. A. High charge-carrier mobility in pi-deficient discotic mesogens: design and structure-property relationship. *Chem. - Eur. J.* **2005**, *11*, 3349. (c) Barlow, S.; Zhang, Q.; kaafarani, B. R.; Risko, C.; Amy, F.; Chan, C. K.; Domercq, B.; Starikova, Z. A.; Antipin, M. Y.; Timofeeva, T. V.; Kippelen, B.; Brédas, J.-L.; Kahn, A.; Marder, S. R.

Synthesis, ionisation potentials and electron affinities of hexaazatrinaphthylene derivatives. *Chem. - Eur. J.* **2007**, *13*, 3537−3547. (d) Sim, R.; Ming, W.; Setiawan, Y.; Lee, P. S. Dependencies of donor−acceptor memory on molecular levels. *J. Phys. Chem. C* **2013**, *117*, 677. (e) Selzer, F.; Falkenberg, C.; Hamburger, M.; Baumgarten, M.; Müllen, K.; Leo, K.; Riede, M. Improved organic p-i-n type solar cells with n-doped fluorinated hexaazatrinaphthylene derivatives HATNA-F_6 and HATNA-F_{12} as transparent electron transport material. *J. Appl. Phys.* **2014**, *115*, No. 054515. (f) Zhao, D.; Zhu, Z.; Kuo, M.-Y.; Chueh, C.-C.; Jen, A. K.-Y. Hexaazatrinaphthylene derivatives: efficient electron-transporting materials with tunable energy levels for inverted perovskite solar cells. *Angew. Chem., Int. Ed.* **2016**, *55*, 8999.

(14) (a) Catalano, V. J.; Larson, W. E.; Olmstead, M. M.; Gray, H. B. Mononuclear and binuclear palladium(II)/rhenium(I) complexes containing a sterically hindered trinucleating Ligand: 2,3,8,9,14,15-Hexamethyl-5,6,11,12,17,18-hexaazatrinaphthalene (hhtn). *Inorg. Chem.* **1994**, *33*, 4502. (b) Piglosiewicz, I. M.; Beckhaus, R.; Saak, W.; Haase, D. Dehydroaromatization of quinoxalines: one-step syntheses of trinuclear 1,6,7,12,13,18-hexaazatrinaphthylene titanium complexes. *J. Am. Chem. Soc.* **2005**, *127*, 14190. (c) Roy, S.; Sarkar, B.; Duboc, C.; Fiedler, J.; Sarper, O.; Lissner, F.; Mobin, S. M.; Lahiri, G. K.; Kaim, W. Heterohexanuclear (Cu_3Fe_3) complexes of substituted hexaazatrinaphthylene (HATN) ligands: twofold BF_4^- association in the solid and stepwise oxidation (3e) or reduction (2e) to spectroelectrochemically characterized species. *Chem. - Eur. J.* **2009**, *15*, 6932. (d) Roy, S.; Kubiak, C. P. Tricarbonylrhenium(I) complexes of highly symmetric hexaazatrinaphthylene ligands (HATN): structural, electrochemical and spectroscopic properties. *Dalton Trans.* **2010**, *39*, 10937. (e) Lind, S. J.; Walsh, T. J.; Blackman, A. G.; Polson, M. I. J.; Irwin, G. I. S.; Gordon, K. C. Trinuclear copper(I) complex containing 3,4,9,10,15,16-hexamethyl-1,6,7,12,13,18-hexaazatrinaphthylene: a structural, spectroscopic, and computational study. *J. Phys. Chem. A* **2009**, *113*, 3566. (f) Fraser, M. G.; Clark, C. A.; Horvath, R.; Lind, S. J.; Blackman, A. G.; Sun, X.-Z.; George, M. W.; Gordon, K. C. Complete family of mono-, bi-, and trinuclear Re(I)$(CO)_3$Cl complexes of the bridging polypyridyl ligand 2,3,8,9,14,15-hexamethyl-5,6,11,12,17,18-hexaazatrinapthalene: syn/anti isomer separation, characterization, and photophysics. *Inorg. Chem.* **2011**, *50*, 6093.

(15) (a) Nie, B.; Zhan, T.-G.; Zhou, T.-Y.; Xian, Z.-Y.; Jiang, G.-F.; Zhao, X. Self-assembly of chiral propeller-like supermolecules with unusual ″sergeants-and-soldiers″ and ″majority-rules″ effects. *Chem. - Asian J.* **2014**, *9*, 754. (b) Li, J.; Chen, S.; Zhang, P.; Wang, Z.; Long, G.; Ganguly, R.; Li, Y.; Zhang, Q. A colorimetric and fluorimetric chemodosimeter for copper ion based on the conversion of dihydropyrazine to pyrazine. *Chem. - Asian J.* **2016**, *11*, 136.

(16) Ibáñez, S.; Poyatos, M.; Peris, E. A D_{3h}-symmetry hexaazatriphenylene-tris-N-heterocyclic carbene ligand and its coordination to iridium and gold: preliminary catalytic studies. *Chem. Commun.* **2017**, *53*, 3733.

(17) (a) Grindell, R.; Vieru, V.; Pugh, T.; Chibotaru, L. F.; Layfield, R. A. Magnetic frustration in a hexaazatrinaphthylene-bridged trimetallic dysprosium single-molecule magnet. *Dalton Trans.* **2016**, *45*, 16556. (b) Gould, C. A.; Darago, L. E.; Gonzalez, M. I.; Demir, S.; Long, J. R. A Trinuclear radical-bridged lanthanide single-molecule magnet. *Angew. Chem., Int. Ed.* **2017**, *56*, 10103. (c) Lemes, M. A.; Magnan, F.; Gabidullin, B.; Brusso, J. Impact of nuclearity and topology on the single molecule magnet behaviour of hexaazatrinaphtylene- based cobalt complexes. *Dalton Trans.* **2018**, *47*, 4678.

(18) (a) Matsunaga, T.; Kubota, T.; Sugimoto, T.; Satoh, M. High-performance lithium secondary batteries using cathode active materials of triquinoxalinylenes exhibiting six electron migration. *Chem. Lett.* **2011**, *40*, 750. (b) Wang, J.; Tee, K.; Lee, Y.; Riduan, S. N.; Zhang, Y. Hexaazatriphenylene derivatives/GO composites as organic cathodes for lithium ion batteries. *J. Mater. Chem. A* **2018**, *6*, 2752.

(19) Bu, X.-H.; Biradha, K.; Yamaguchi, T.; Nishimura, M.; Ito, T.; Tanaka, K.; Shionoya, M. A novel polymeric Ag^I complex consisting of two three-dimensional networks which are enantiometric and interpenetrating. *Chem. Commun.* **2000**, 1953.

(20) Wöhrle, T.; Wurzbach, I.; Kirres, J.; Kostidou, A.; Kapernaum, N.; Litterscheidt, J.; Haenle, J. C.; Staffeld, P.; Baro, A.; Giesselmann, F.; Laschat, S. Discotic liquid crystals. *Chem. Rev.* **2016**, *116*, 1139.

(21) McKeown, N. B.; Gahnem, B.; Msayib, K. J.; Budd, P. M.; Tattershall, C. E.; Mahmood, K.; Tan, S.; Book, D.; Langmi, H. W.; Walton, A. Towards polymer-based hydrogen storage materials: engineering ultramicroporous cavities within polymers of intrinsic microporosity. *Angew. Chem., Int. Ed.* **2006**, *45*, 1804.

(22) Xu, F.; Chen, X.; Tang, Z.; Wu, D.; Fu, R.; Jiang, D. Redox-active conjugated microporous polymers: a new organic platform for highly efficient energy storage. *Chem. Commun.* **2014**, *50*, 4788.

(23) Xiao, R.; Tobin, J. M.; Zha, M.; Hou, Y.-L.; He, J.; Vilela, F.; Xu, Z. A nanoporous graphene analog for superfast heavy metal removal and continuous-flow visible-light photoredox catalysis. *J. Mater. Chem. A* **2017**, *5*, 20180.

(24) Yuan, F.; Li, J.; Namuangruk, S.; Kungwan, N.; Guo, J.; Wang, C. Microporous, self-segregated, graphenal polymer nanosheets prepared by dehydrogenative condensation of aza-PAHs building blocks in the solid state. *Chem. Mater.* **2017**, *29*, 3971.

(25) (a) Yamakata, M.; Goto, S.; Uruga, T.; Takeshita, K.; Ishikawa, T. Optical design of BL02B2 bending magnet beamline at the SPring-8 for powder diffraction. *Nucl. Instrum. Methods Phys. Res., Sect. A* **2001**, *467−468*, 667−669. (b) Nishibori, E.; Takata, M.; Kato, K.; Sakata, M.; Kubota, Y.; Aoyagi, S.; Kuroiwa, Y.; Yamakata, M.; Ikeda, N. The large Debye-Scherrer camera installed at SPring-8 BL02B2 for charge density studies. *Nucl. Instrum. Methods Phys. Res., Sect. A* **2001**, *467−468*, 1045−1048. (c) Kawaguchi, S.; Takemoto, M.; Osaka, K.; Nishibori, E.; Moriyoshi, C.; Kubota, Y.; Kuroiwa, Y.; Sugimoto, K. High-throughput powder diffraction measurement system consisting of multiple MYTHEN detectors at beamline BL02B2 of SPring-8. *Rev. Sci. Instrum.* **2017**, *88*, No. 085111.

(26) (a) Nishide, H.; Takahashi, M.; Takashima, J.; Pu, Y.-J.; Tsuchida, E. Acyclic and cyclic di- and tri(4-oxyphenyl-1,2-phenyleneethynylene)s: their synthesis and ferromagnetic spin interaction. *J. Org. Chem.* **1999**, *64*, 7375. (b) Tehfe, M.-A.; Dumur, F.; Xiao, P.; Zhang, J.; Graff, B.; Morlet-Savary, F.; Gigmes, D.; Fouassier, J.-P.; Lalevée, J. Photoinitiators based on a phenazine scaffold: high performance systems upon near-UV or visible LED (385, 395 and 405 nm) irradiations. *Polymer* **2014**, *55*, 2285. (c) Gomez, E.; Gutierrez, M.; Moreno, M.; Hisaki, I.; Nakagawa, S.; Douhal, A. *Phys. Chem. Chem. Phys.* **2018**, *20*, 7415. (d) Gomez, E.; Gutiérrez, M.; Cohen, B.; Hisaki, I.; Douhal, A. Spectroscopy and dynamics of dehydrobenzo[12]annulene derivatives possessing peripheral carboxyphenyl groups: theory and experiment. *J. Mater. Chem. C* **2018**, *6*, 6929−6939. (e) Wang, J.; Lee, Y.; Tee, K.; Riduan, S. N.; Zhang, Y. A nanoporous sulfur-bridged hexaazatrinaphthylene framework as an organic cathode for lithium ion batteries with well-balanced electrochemical performance. *Chem. Commun.* **2018**, *54*, 7681.

(27) Organero, J. A.; Tormo, L.; Douhal, A. Caging ultrafast proton transfer and twisting motion of 1-hydroxy-2-acetonaphthone. *Chem. Phys. Lett.* **2002**, *363*, 409.

(28) (a) Reshchikov, M. A.; Morkoç, H. Luminescence properties of defects in GaN. *J. Appl. Phys.* **2005**, *97*, No. 061301. (b) Fang, Z.; Bueken, B.; De Vos, D. E.; Fischer, R. A. Defect-engineered metal-organic frameworks. *Angew. Chem., Int. Ed.* **2015**, *54*, 7234. (c) Gutiérrez, M.; Martin, C.; Kennes, K.; Hofkens, J.; Van der Auweraer, M.; Sánchez, F.; Douhal, A. OLEDs Based on metal-organic framework: new OLEDs based on zirconium metal-organic framework. *Adv. Opt. Mater.* **2018**, *6*, 1701060.

(29) Dhakshinamoorthy, A.; Li, Z.; Garcia, H. Catalysis and photocatalysis by metal organic frameworks. *Chem. Soc. Rev.* **2018**, *47*, 8134.